Journal

Forecasting phase-field variable in brittle fracture problems by autoregressive integrated moving average technique

Cuong T. Nguyen [1,*], Long H. Le[2], Minh N. Dinh[1], Ngoc M. La[1]
[1] *School of Science, Engineering, and Technology, RMIT University Vietnam, Vietnam*
[2] *Automotive R&D Center, Bosch Vietnam, Vietnam*

Received (Day Month Year)
Revised (Day Month Year)

Phase-field modeling is a powerful and versatile computational approach for modeling the evolution of cracks in solids. However, phase-field modeling requires high computational cost for capturing accurately how cracks develop under increasing loads. In brittle fracture mechanics, the crack initiation and propagation can be considered as a time series forecasting problem so they can be studied by observing the change of the phase-field variable, which represents the level of material damaging. In this paper, we develop a rather simple approach utilizing autoregressive integrated moving average technique (ARIMA) to predict the variation of the phase-field variable in an isothermal, linear elastic and isotropic phase-field model for brittle materials. Time series data of the phase-field variable is extracted from numerical results using coarse finite-element meshes. Two ARIMA schemes are introduced to exploit the structure of the collected data and provide a prediction for the change of phase-field variable when using a finer mesh, that gives a better results in terms of accuracy but it requires highly computational cost.

Keywords: fracture mechanics; bittle fracture; phase-field modelling; time-series forecasting.

1. Introduction

Fracture is one of the main failure modes of engineering materials and structures. Predicting the nucleation and propagation of cracks is, therefore, a great importance in engineering analysis and design. Theoretical foundations to understand brittle crack evolution was introduced and outlined in the works of [Griffith (1921)], [Irwin (1921)] and [Barenblatt (1962)]. Following Griffith and Irwin, crack propagation can be considered as a stability problem, in which if the energy release rate reaches a critical value the crack starts to propagate. The Griffith theory describes an adequate criterion for crack propagation, but is insufficient to determine curvilinear crack paths, crack kinking and benching.

*Corresponding author: cuong.nguyentan@rmit.edu.vn

Numerical approaches to fracture problems can be categorized as discontinous crack and smeared crack models. In the former approach, cracks are presented as discrete entities with discontinuous displacement field across the crack line (in 2D) or surface (in 3D). Representative methods in this approach can be listed are extended finite element methods (XFEM), [Moës (1999)] and remeshing strategies, [Branco (2015)]. With these methods, the task of tracking crack paths may be impossible in problems with complex crack patterns and the extension to complex three-dimensional problems is also nontrivial. Phase-field modeling (PFM by [Francfort (1998)] and [Miehe (2010)]) uses smeared crack models as an alternative. In this model, the discontinuity in the material is assumed to be not sharp, but is *smeared* over a localisation band. This spatially diffuse fracture zone is coupled with an additional continuous field variable, which we refer to as the phase-field variable. Mathematically speaking, PFM can be considered as a tool for solving fracture mechanics problems using partial differential equations (PDEs): one solves two PDEs, one for the vectorial displacement field and the other for the scalar phase-field. The advantage of PFM compared with FEM and XFEM is that PFM can handle complex crack shapes by changing the phase-field value on a fixed mesh. By doing so, in PFM there is no need to remesh when cracks propagate like FEM and XFEM. Therefore, the computational time and cost are greatly reduced without the risk of losing accuracy. However, PFM is still essentially a mesh-based method, so the mesh quality has a significant effect on the obtained results.

One of the main drawbacks of PFM is its highly computational cost. Specifically, in order to capture the crack phenomenon accurately a sufficiently refined mesh surrounding the crack tip is required. In this work we propose a rather simple approach based on a time-series forecasting technique in machine learning to go around this issue by using the phase-field results of coarse meshes to predict the corresponding result of the finer mesh. In machine learning, in order to deal with time-dependent variables there are two main approaches: statistical methods and artificial neural networks. Given a time series, Holt-Winters [Gardner (1985)] forecasting models the three exponentially weighted moving average (EWMA) aspects including the average value, the trend over time, and the seasonality. The model makes predictions by computing the combined effects of these three factors. On the other hand, the autoregressive integrated moving average (ARIMA) framework [Brockwell (2002)] models how each data point in the time series is influenced by its previous values (auto-regressive), and integrates that knowledge with a moving average part, which computes the linear combination of several data points, to make predictions. As a result, Holt-Winters works better for seasonal time series while ARIMA works better for non-stationary time series. In this paper, PFM is used to build a model for brittle fracture problems based on the theoretical fracture model of Griffith. The results of PFM for the coarse mesh of brittle fracture plate with three successively coarse meshes are used as a database. Then, ARIMA will be employed to forecast the outcome of the finer mesh along the way of refining finite-element meshes. Next, the predicted results will be compared with the true data obtained using PFM with the actual discretization in the finer mesh.

The paper is structured as follows. Section 2 is dedicated to the overview of phase-field framework for brittle fracture problems, a series of representative numerical examples is also examined for the purpose of generating data and then verifying our predictions. In Section 3.1 we present a brief review of ARIMA as a time-series forecasting. Our main contributions are presented in Section 3.2, in which we propose two ARIMA schemes for predicting the phase-field variable. The accuracy and efficiency of the two proposed schemes are illustrated in Section 4.

2. Phase-field modeling of brittle fracture

We begin by reviewing the theoretical foundation of brittle fracture mechanics and the phase-field modeling approach. Then, in Section 2.5 we present a series of numerical examples covering both two-dimensional and three-dimensional brittle fracture problems.

2.1. *Griffith's theory and the variational approach*

The theory of Linear Elastic Fracture Mechanics was born in 1920 by [Griffith (1921)]. In his approach, the competition between the bulk energy away from the crack and the surface energy on the crack results in crack propagation. The stress intensity factor approach introduced by [Irwin (1921)] focuses on the stress state around the crack tip is also a useful method in engineering practice.

We consider a body occupying in the domain $\Omega \subset \mathbb{R}^n$ with the spatial dimension $n \in \{1, 2, 3\}$ and a crack set $\Gamma \subset \mathbb{R}^{n-1}$ is included. Under this problem setting, the total energy functional is given by

$$\mathcal{E} := \Psi_s - \mathcal{W} + \Psi_c, \tag{1}$$

where the stored strain energy, the external work, and the surface energy are defined as

$$\Psi_s(\mathbf{u}) = \int_{\Omega\backslash\Gamma} \psi(\boldsymbol{\epsilon}(\mathbf{u}), \Gamma) dV, \quad \mathcal{W} = \int_{\Omega} \mathbf{b}^* \cdot \mathbf{u} dV + \int_{\partial\Omega_t} \mathbf{t}^* \cdot \mathbf{u} dA, \ \Psi_c(\Gamma) = \int_{\Gamma} g_c dA, \tag{2}$$

g_c being the critical energy release rate or the fracture toughness. The global minimiser of this potential energy functional $\mathcal{E}$ leads to the solution of the problem under consideration

$$(\mathbf{u}(t), \Gamma(t)) = \arg\{\min \mathcal{E}(\mathbf{u}, t)\}. \tag{3}$$

This problem is essentially a *moving* boundary value problem since Γ_c changes versus time. In order to overcome the difficulty due to the moving boundary, the surface integral is replaced by a volume integral as follows [Bourdin (2008)]

$$\psi_c = \int_{\Gamma} g_c dA \approx \int_{\Omega} g_c \gamma dV, \tag{4}$$

where γ is the the crack density, which depends on a length-scale parameter l_c and the continuous scalar-valued phased-field ϕ. These quantities will be discussed in detail the subsequent sections.

2.2. *Phase-field approximation with a diffusive crack topology*

For quasi-static brittle fracture of isotropic elastic solids, the cracks are approximated as finite bands captured by a crack phase-field variable ϕ: $\phi = 1$ denotes the fully broken material and $\phi = 0$ represents the intact one. To illustrate the idea behind the concept of a diffuse crack topology, it is ideal to consider an infinite bar of cross-section Γ aligned along the x-axis [Miehe (2010)]. The domain under consideration is $\mathcal{B} = \Gamma \times L$, where $L = (-\infty, +\infty)$ and position $x \in L$. A fully opened crack is specified at $x = 0$. The sharp crack profile can be described by the phase-field variable $\phi(x) \in [0, 1]$ with

$$\phi(x) := \begin{cases} 1 & \text{for } x = 0 \\ 0 & \text{otherwise} \end{cases} \tag{5}$$

Following the physical observation that the crack itself initiates with micro-cracks and nano-voids, it is essentially not a discrete phenomenon, the non-smooth phase-field is replaced by a smeared counterpart defined by the following exponential function

$$\phi(x) = e^{-|x|/l_c}, \tag{6}$$

where l_c is the length scale parameter. We observe that $\phi(x) = e^{-|x|/l_c}$ is the solution of the homogeneous second-order differential equation

$$\phi(x) - l_c^2 \phi''(x) = 0. \tag{7}$$

subject to Dirichlet boundary conditions $\phi(0) = 1,\ \phi(\pm\infty) = 0$ since the solution of the associated characteristic equation $1 - l_c^2 s^2 = 0$ is given by $s = \pm 1/l_c$. The corresponding variational principle of this Euler equation can be written as

$$\phi = \arg\left\{ \inf_{\phi \in W} I(\phi) \right\},\ \text{where } I(\phi) = \frac{1}{2} \int_\Omega (\phi^2 + l_c^2 \phi'^2) dV, \tag{8}$$

and $W = \{\phi | \phi(0) = 1,\ \phi(\pm\infty) = 0\}$. Substituting $dV = \Gamma dx$ into the expression of the functional $I(\phi)$ leads to $I(\phi = e^{-|x|/l_c}) = l_c \Gamma$. Then, we define the fracture surface density

$$\Gamma(\phi) = \frac{I(\phi)}{l_c} = \frac{1}{2l_c} \int_B (\phi^2 + l_c^2 \phi'^2) dV = \int \gamma(\phi, \phi') dV, \quad \gamma(\phi, \phi') = \frac{1}{2l_c}\phi^2 + \frac{l}{2}\phi'^2. \tag{9}$$

2.3. *Strain energy degradation*

The formulation for cracks in multi-dimensional solids can be obtained in a straightforward manner by extending the formula for one-dimensional solids presented in the preceding section. Specifically, replacing the ordinary derivative ϕ' by the gradient $\nabla\phi$ leads to the *crack surface density function* per unit volume of a multi-dimensional solid

$$\gamma(\phi, \phi') \to \gamma(\phi, \nabla\phi) = \frac{1}{2l_c}\phi^2 + \frac{l_c}{2}\nabla\phi^2.$$

Then, the surface energy Ψ_c is approximated as

$$\Psi_c = \int_\Gamma g_c d\Gamma \approx \int_\Omega g_c \gamma(\phi, \nabla\phi) dV.$$

Due to the damage by cracks, the elastic energy is degraded with function $g(\phi)$

$$\psi(\boldsymbol{\epsilon}, \phi) = g(\phi)\psi_0(\boldsymbol{\epsilon}),$$

where $g(\phi)$ is the degradation function. There are many choices for function $g(\phi)$, but we choose the most basic one $g(\phi) = (1-\phi)^2+\kappa$ introduced by [Bourdin (2008)], in which κ is a small number responsible for keeping the system of equations stable. Then, the total internal energy can be approximated as:

$$\Psi = \Psi_s + \Psi_c \approx \int_\Omega \left[((1-\phi)^2 + \kappa)\psi_0(\boldsymbol{\epsilon}) + g_c\gamma(\phi, \nabla\phi)\right] dV,$$

we have used a so-called history variable $H = \max(\psi_0(\boldsymbol{\epsilon}), H_n)$, in which H_n is the computed energy history at the previous step n [Molnár (2017)]. It enforces the irreversibility of the damage $\dot{\phi} \geq 0$, which leads to the Karush-Kuhn-Tucker conditions [Singh (2016)]:

$$\dot{H} \geq 0, \quad \psi_0 - H \leq 0, \quad \dot{H}(\psi_0 - H) = 0. \tag{10}$$

2.4. *Finite element implementation*

Within the finite-element framework, the displacement $\mathbf{u}$ and the phase-field variable ϕ are discretized using the standard Galerkin method [Hughes (2012)] as follows

$$u_i^h = \sum_{A=1}^{n_b} N^A u_i^A, \qquad \phi_i^h = \sum_{A=1}^{n_b} N^A \phi_i^A, \tag{11}$$

where n_b is the dimension of the discrete space, N^A are the basis functions, and u_i^A and ϕ^A are the nodal degrees-of-freedom for the displacement and phase-field. Taking the variation of two energies ($\delta\Psi = \delta\Pi^u = 0$, where $\Pi^u = \Psi_s - \mathcal{W}$) and adopting a staggered solution scheme, we arrive at a combined system of equations

$$\begin{cases} \phi_{n+1} = \arg\left\{\inf\limits_u \int\limits_\Omega \left[g_c\gamma\left(\phi, \nabla\phi\right) + (1-\phi)^2 H\right] dV\right\} \to \mathbf{K}_n^u \phi_{n+1} = -\mathbf{r}_n^\phi \\ \mathbf{u}_{n+1} = \arg\left\{\inf\limits_u \int\limits_\Omega \left[\psi\left(\mathbf{u}, \phi_n\right) - \mathbf{b}^* \cdot \mathbf{u}\right] dV - \int\limits_{\partial\Omega} \mathbf{t}^* \cdot \mathbf{u} dA\right\} \to \mathbf{K}_n^u \mathbf{u}_{n+1} = -\mathbf{r}_n^u \end{cases}, \tag{12}$$

where the tangent stiffness matrices for the displacement and phase-field solutions are computed as

$$\begin{cases} \mathbf{K}^u = \int_\Omega \left\{ \left[(1-\phi)^2 + \kappa\right] \mathbf{B}^T \mathbf{C}_0 \mathbf{B} \right\} dV \\ \mathbf{K}^\phi = \int_\Omega \left\{ \left[g_c/l_c + 2H\right] \mathbf{N}^T \mathbf{N} + g_c l_c \mathbf{B}^T \mathbf{B} \right\} dV \end{cases}, \tag{13}$$

and the residuals are given by

$$\begin{cases} \mathbf{r}^u = \mathbf{f}_{int} - \mathbf{f}_{ext} = \int_\Omega b^* \cdot \mathbf{N}^T dV + \int_{\partial\Omega_t} t^* \cdot \mathbf{N}^T dA \\ \mathbf{r}^\phi = \left\{ \left[g_c \phi/l_c - 2(1-\phi)H\right] \mathbf{N}^T + g_c l_c \mathbf{B}^T \nabla\phi \right\} dV \end{cases}, \tag{14}$$

where $\mathbf{N} = [N^A], A = 1, 2, \ldots, n_b$ is the row vector of shape functions and $\mathbf{B}$ is a matrix of the spatial derivatives.

2.5. *Representative numerical examples*

In this section we present several numerical examples in which phase-field data is generated by using the phase-field model for the purpose of training and testing our machine learning algorithms. We first start with a benchmark test of only one element in plane-strain. Then numerical experiments for a single edge notched plate in tension, shear and mixed modes are carried out to obtain the phase-field time series at the crack tip. A tensile test of a plate with two notches arranged symmetrically is also studied. Finally, we examine a three-dimensional problem in tensile loading.

2.5.1. *Benchmark test*

In order to verify the numerical results produced by our phase-field modeling, we consider a two-dimensional element in plane strain, which is depicted in Figure 1. Geometric dimensions and material properties are summarized in Table 1. The bottom nodes are constrained in both directions while the top nodes are free to slide vertically. The prescribed displacement v is applied in 1000 steps, where the increment in each step $\Delta v = 10^{-4}$ mm. This example is served as a benchmark test since its analytical solution exists so we are able to verify our numerical results. The exact solution describing the relation of the phase-field and the vertical strain is given by

$$\phi(\varepsilon_y) = \frac{\varepsilon_y^2 l_c c_{22}}{g_c + \varepsilon_y^2 l_c c_{22}}. \tag{15}$$

In which, c_{22} is the entry in row 2 and column 2 of the stiffness matrix $\mathbf{C}_0$, it can be computed as

$$c_{22} = \frac{E(1-\nu)}{(1+\nu)(1-2\nu)}. \tag{16}$$

Once the exact phase-field $\phi(\varepsilon_y)$ is determined, the vertical stress is related to the phase-field as

$$\sigma_y = c_{22}\varepsilon_y \left[1 - \phi(\varepsilon_y)\right]^2 . \tag{17}$$

The variations of phase-field variable and stress versus the vertical strain are plotted in Figure 2. As can be seen from this Figure, the numerical solution obtained by phase-field modeling matches pretty well with the analytical one.

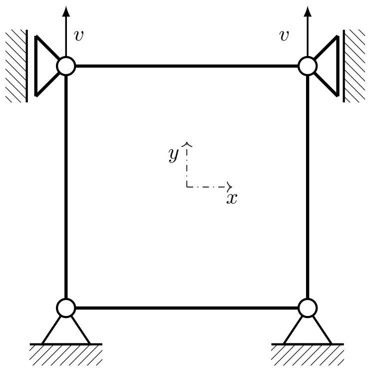

Fig. 1: One-element problem.

Table 1: Parameters used in one-element problem.

Dimensions	Young's modulus	Poisson's ratio	The critical energy release rate	Length scale
1 mm × 1 mm	$E = 210$ kN/mm^2	$\nu = 0.3$	$g_c = 5 \times 10^{-3}$ kN/mm	$l_c = 0.1$ mm

2.5.2. *Single edge notched and symmetric double notched tensile tests*

Next, we consider the well known single edge notched tension test. The geometry and the boundary conditions of a squared plate are depicted in Figure 3 (left). There is an initial notch in the horizontal direction at middle height from the left edge of the plate to its center. Material parameters are specified similarly as in the one-element example (Section 2.5.1)), except that $g_c = 2.7 \times 10^{-3}$ kN/mm and the length scale is chosen as $l_c = 4h$, where h is the element size. The loading is applied with $\Delta u = 5 \times 10^{-5}$ mm.

In this example, the specimen is discretized with four finite–element mesh sizes in the order of gradually increasing number of elements as 1600 (40 × 40), 2500 (50 × 50), 3600 (60 × 60) and 4900 (70 × 70). We examine three cases representing

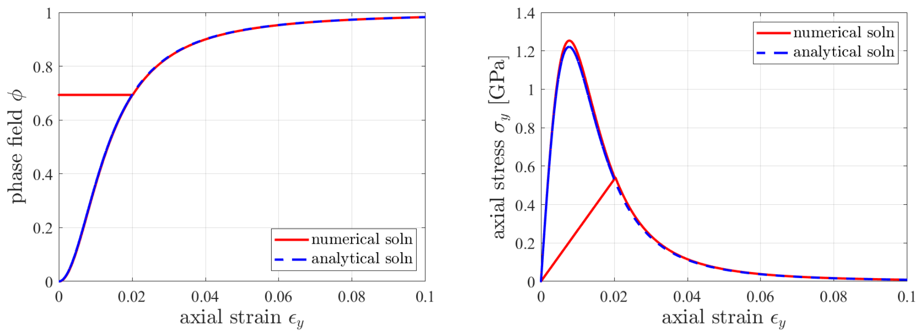

Fig. 2: One-element problem: phase-field ϕ (left) and axial stress σ_y (right) versus axial strain ε_y.

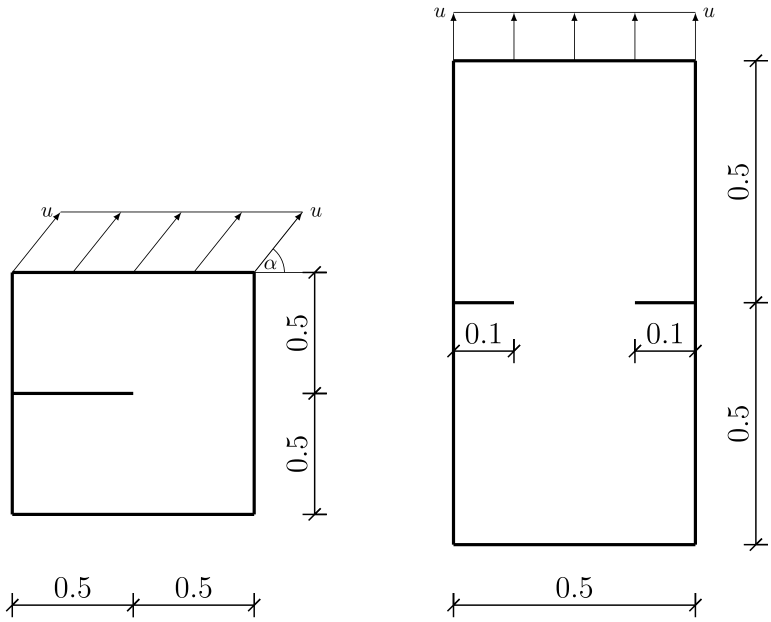

Fig. 3: Two-dimensional problems: single-edge-notched specimen (left) and double-notched specimen (right).

three typical failure modes in two-dimensional fracture problems: $\alpha = 90°$ (mode I - tension), $\alpha = 0$ (mode II - pure shear), and $\alpha = 45°$ (mixed mode). The evolution of the phase-field variable at the crack tip in these problems is plotted in Figure 4. In the symmetric double notched tensile test shown in Figure 3 (right), the length of the vertical side of the specimen is twice that of the horizontal one so four meshes are specified as $40 \times 80, 50 \times 100, 60 \times 120$ and 70×140. The displacement control

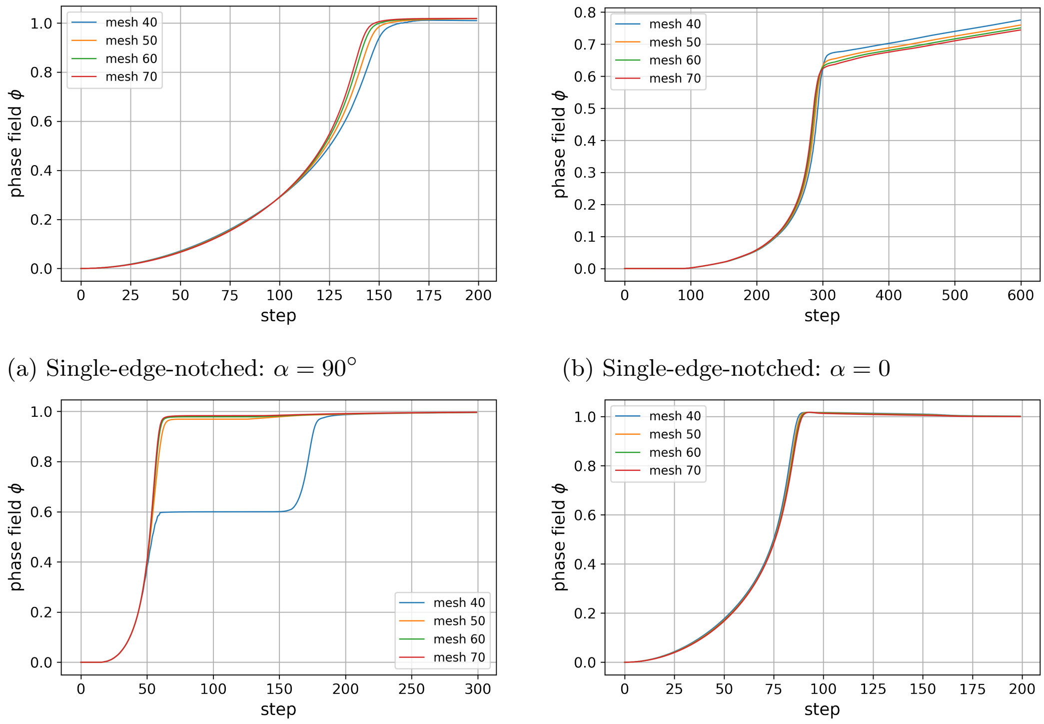

(a) Single-edge-notched: $\alpha = 90^\circ$

(b) Single-edge-notched: $\alpha = 0$

(c) Single-edge-notched: $\alpha = 45^\circ$

(d) Symmetric-doubled-notched

Fig. 4: Variations of phase-field variable in two-dimensional problems.

loading is applied in $N = 200$ steps with the increment $\Delta v = 10^{-4}$ mm.

As can be seen from Figure 4, there are clear trends of the phase-field value in four mesh sizes of these problems. Specifically, the value of phase-field variable changes and tends to get convergence as refining the mesh. In principle, the results will be more accurate when decreasing the mesh size. However, refining the mesh leads to a significant increase in the computational cost. Instead of using the finer mesh, we predict the variation of the phase-field variable using time-series modeling techniques, which will be discussed in detail in Section 3.2. The idea is to utilize coarse-grain crack propagation data and train ARIMA models for predicting the results of the most finer mesh.

2.5.3. *Three dimensional single notched test*

We consider the three-dimensional setting tensile test specimen depicted in Figure 5 The bottom face is constrained and the top face is subject to an uniformly prescribed displacement $\Delta u = 10^{-3}$ mm for $N = 1000$ steps. The material properties and geometric dimensions are chosen according to Ref. [Miehe (2010)], summarized in

Table 2.

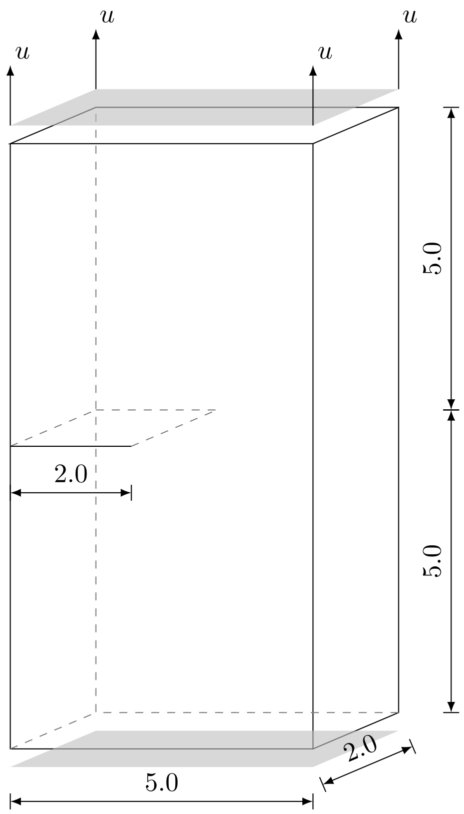

Fig. 5: Three-dimensional single notched test.

Table 2: Parameters used in the three dimensional single notched test.

Dimensions	Young's modulus	Poisson's ratio	The critical energy release rate	Length scale
5 mm × 10 mm × 2 mm	$E = 20.8$ kN/mm^2	$\nu = 0.3$	$g_c = 5 \times 10^{-4}$ kN/mm	$l_c = 4h$

3. ARIMA

This section presents our proposed training algrithms implementing ARIMA technique. We start with a brief review of ARIMA as a time-series forecasting in Section

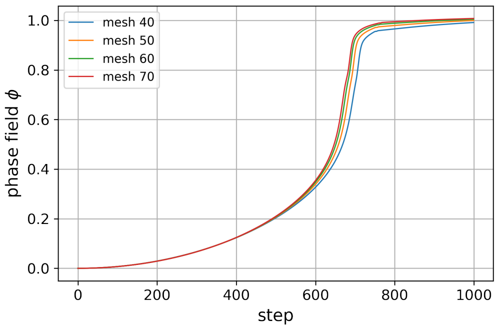

Fig. 6: Variations of phase-field variable in the three-dimensional problem.

3.1. Then we will introduce two ways of training using ARIMA in predicting the phase-field variable in Section 3.2. The phase-field value changes and tends to converge as the mesh size increases, it is more accurate when increasing the mesh size. We investigate how crack propagation can be predicted using time-series modeling techniques.

3.1. *ARIMA as a time-series forecasting*

A time-series composes of past observations which can be mined to discover internal structures such as autocorrelation, trend, and seasonal variation. Furthermore, such insights can be used to deliver monitoring and prediction capacities. If we consider a time-series with past observations as a discrete variable where X_t denotes the observation instance and t denotes the zero-mean random noise term at time t. We establish an autoregression model (AR) such as:

$$X_t = \sum_{i=1}^{k} \alpha_i X_{t-i} + \epsilon_t \tag{18}$$

Then, the noise term is presented using a Moving Average (MA) model such as:

$$X_t = \sum_{i=1}^{q} \beta_i \epsilon_{t-i} + \epsilon_t \tag{19}$$

To fit a best model for the time-series given independent noise terms, the autoregressive moving average (ARMA) framework [Hamilton (2020)] integrates the linear function of the previous time steps with the independent random noise minus a fraction of the previous random noise. ARMA model takes two parameters (k, q):

- k - “autoregressive” term: presents the lags of the series in the prediction process;

- q - The "moving average" term: presents the lags of the forecast errors.

Nonetheless, ARMA cannot be used effectively for non-stationary time-series. To address this drawback, the autoregressive integrated moving average (ARIMA) framework, an extension of ARMA, integrates the differencing of past observations (at consecutive time steps) to "stationarize" the time series before applying the standard ARMA scheme [Brockwell (2002)]. As a result, the ARIMA framework includes the parameter d, capturing the differencing level. The complete ARIMA scheme is described as follow:

A random variable is considered a stationary time series if its statistical properties such as first and second moments are approximately constant over time. Visualizing a stationary series shows data points vary around its mean with a relatively constant amplitude. The autoregressive integrated moving average (ARIMA) framework, an extension of ARMA, addresses this limitation by integrating the differencing of raw observations to allow the time series to become stationary [Brockwell (2002)]. Accordingly, the ARIMA framework introduces an extra parameter d, and performs time series forecasting for nonstationary series as follow:

$$\begin{aligned} \nabla^d X_t &= \epsilon_t + \sum_{i=1}^{k} \alpha_i \nabla^d X_{t-i} + \sum_{i=1}^{q} \beta_i \epsilon_{t-i} \\ \tilde{X}_t &= \nabla^d \tilde{X}_t + \sum_{i=1}^{d-1} \nabla^i X_{t-i} \end{aligned} \tag{20}$$

To conclude, an ARIMA (k, d, q) forecasting model not only performs the "signal filtering" act but also the "trend filtering" act by applying the $d^{\text{th}}-$ order differencing, inducing past observations into future forecasts.

Considering our brittle fracture analysis process as a time-series, we need to determine these parameters (k, d, q) to construct an ARIMA forecasting model. First, because computational simulations such as the Isotropic Brittle Fracture Model do not generate noise, we argue that q can be set to zero. Second, as the original time series is not stationary, we need to do a stationary study to see what level of order-difference for our time-series. We discuss how to identify suitable values for parameters d and k below.

- k: the number of autoregressive terms (i.e. the lagged value);
- d: the number of differences needed for stationarity;
- q: the noise term.

(1) Order of differencing d
A stationary time-series means no orders of differencing is needed and thus $d = 0$. Our study shows that our time-series is non-stationary and the order of differencing (essential for our ARIMA model) can be computed as followed,

where Δd denotes the d^{th} difference of time series X, we define the following differencing levels:

$$d = 1 : \Delta_t^1 = X_t - X_{t-1} \tag{21}$$

$$d = 2 : \Delta_t^2 = (X_t - X_{t-1})(X_{t-1} - X_{t-2}) \tag{22}$$

Referring to [Dinh (2022)], we detect a constant increasing/decreasing trend in our original time series. Further study shows that one order of differencing (i.e., $d = 1$) stationarizes our target time series so that the ARMA process can be conducted to perform forecasting of the phase-field values over time.

(2) Number of autoregressive terms k
Our time-series analysis framework handles sequentialobservations at every time-step and updates the forecasting buffer simultaneously. This is a conventional approach for many time-step based applications, and $k = 1$ (i.e. AR(1)) is applicable to our ARIMA model.

As a result, we study aninitial ARIMA(1,1,0) model which can be described as "the differenced first-order auto-regressive model". To conclude, this ARIMA model regresses the first difference of a collection of observable phase-field values as a non-stationary time series, with the lag value of one period.

3.2. *ARIMA for phase-field forecasting*

As can be seen in Section 2.5, the change of phase-field variable versus the precribed displacement step can be considered as time-series data. Therefore, ARIMA is a promising candidate, which can be used to train the collected data from coarse meshes and provide a prediction on the results of the finer mesh. In this section, we present two training ways using ARIMA for predicting phase-field variable of problems presented in the preceding section. The numerical results using the finest mesh in each example is considered as the most accurate one among the given four mesh grids. Our purpose is to use the results of three coarser meshes, e.g. 40×40, 50×50 and 60×60 for predicting the results of mesh 70×70 in the single edge notched test example.

3.2.1. *Out-of-time training (ARIMA1)*

The data of the phase-field variable at the crack tip using various mesh sizes are collected and divided into two folds including training and testing. In this model, we use the complete result of a based mesh, it can be mesh 40, mesh 50, or mesh 60 and a part $R\%$ of mesh70 to predict its own remaining part, i.e. $(100 - R)\%$. After being trained using full data of the based mesh and the training part of the fine mesh, the remaining part of the fine mesh will be predicted. Figure 7 describes the process of training in detail.

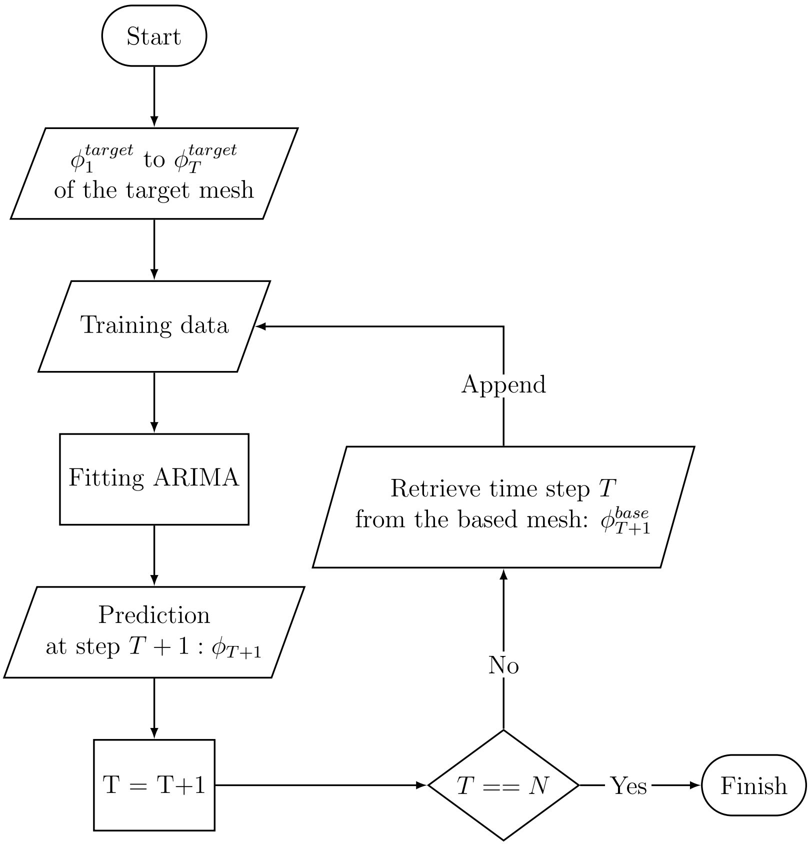

Fig. 7: ARIMA1: Out-of-time training process.

3.2.2. *Across-grids training (ARIMA2)*

The advantage of out-of-time forecasting ARIMA presented in Section 3.2.1 is that the accuracy can be improved proportionally with the size $R\%$ of the training data. However, in many cases, the partition data of the highly accurate results (mesh 70) does not exist. In addition, the accuracy of ARIMA1 is limited since the trend is strongly affected by the chosen based mesh. ARIMA2 is introduced to overcome these weaknesses. In particular, in ARIMA2 we use the full data of the three coarse meshes, which can be achieved easily as the database to predict the fine mesh solution. We consider the phase-field variable across meshes at each step as a short-time time-series. It is clear that it has a trend converging to the exact solution when the mesh gets finer. We assume that the phase-field prediction in the next finer mesh at the same loading step can be represented as a linear function of the differenced phase-field values and residual errors at coarser meshes. At each step,

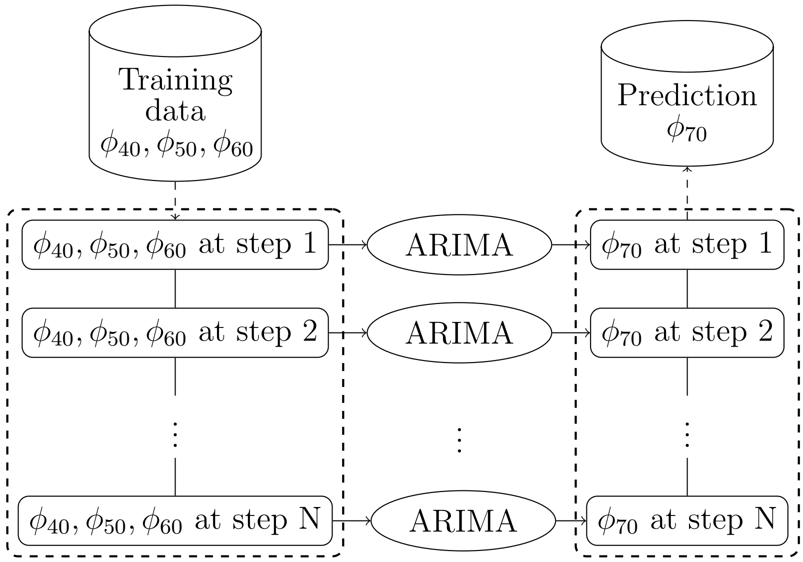

Fig. 8: ARIMA2: Across-grids training process.

we go across size grids, we train an ARIMA model based on the corresponding results of meshes 40, 50 and 60, then produce a prediction for the mesh 70. It is clear that with this training way we are predicting a short-time series so it is better to update the order of moving-average model $q = 1$. The detailed training process is illustrated in Figure 8.

3.2.3. *Performance assessment metric*

In assessing the accuracy of prediction obtained by forecasting models the root-mean-square error (RMSE) is used frequently. It measures the difference between the predicated values and the ground truth in L_2 norm and is defined as follows

$$RMSE = \sqrt{\frac{1}{N}\sum_{i=1}^{N}(x_i - \hat{x}_i)^2}, \tag{23}$$

where N being the total number of observations, x_i is the actual value and $\hat{x}_i$ is the predicted one. The reason for using RMSE is that it penalizes large errors, thus helps us rank the performance of the forecasting techniques.

4. Predictive results

4.1. *Training and predicting the phase-field variable*

As can be seen in Table 3, the errors when using ARIMA1 get smaller when the based mesh is chosen closer to the predictive mesh. The more true data we use (the higher value of R), the more accurate the results is observed. Figure 9 shows the prediction of the phase-field of mesh 70 with the training set $R = 60\%$ and the based mesh is 60. The prediction matches fairly well with the ground data of running the mesh 70. In overall, we can see that ARIMA2 gives a better agreement in comparison with ARIMA1. The enhancement in accuracy can be explained relying on the data structures in two training algorithms. In ARIMA2, the training data is structured as *short-term* data series, which can take benefits of ARIMA models. In short, the ARIMA2 model with the across-grids approach gives better results in most cases without using any part of the finest mesh data.

4.2. *Training and predicting the reaction force by ARIMA2*

When comparing the two ARIMA schemes in predicing the phase-field variable, we observed that ARIMA2 performs outstandingly. Therefore, we proceed to investigate its ability to predict the reaction force. It turns out that ARIMA2 also performs very well in this predictive task. As we can see in Table 3, the RMSE when using ARIMA2 is always less than 0.008.

5. Conclusion

In this study, the time series approach based on ARIMA models is ultilized to train and predict the numerical results obtained by using phase-field modeling for brittle fracture problems. Numerical examples ranging from two-dimensional to three-dimensional problems are presented to show the performance of the two proposed ARIMA schemes in predicing the phase-field variable. The results show that it is feasible to use data from coarse meshes to predict the value of phase-field variable in a denser mesh size, especially with ARIMA2 scheme. The application of ARIMA2 is also valid for predicting the reaction force.

Table 3: RMSE results of two ARIMA approaches.

Problem		ARIMA1 (Phase-field ϕ)			ARIMA2	
	Base	30%	40%	50%	Phase-field ϕ	Reaction force F
Tension ($\alpha = 90°$)	Mesh 40	0.044941	0.044861	0.044815	0.001555	0.003952
	Mesh 50	0.023772	0.023730	0.023647		
	Mesh 60	0.009785	0.009726	0.009733		
Pure shear ($\alpha = 0$)	Mesh 40	0.028423	0.028114	0.021058	0.001943	0.002317
	Mesh 50	0.014916	0.014544	0.010444		
	Mesh 60	0.006528	0.006635	0.004422		
Mixed modes ($\alpha = 45°$)	Mesh 40	0.199574	0.158567	0.102213	0.003474	0.007625
	Mesh 50	0.005951	0.004003	0.001696		
	Mesh 60	0.002123	0.001524	0.000766		
Double-notch	Mesh 40×80	0.015644	0.009836	0.003424	0.002657	0.005326
	Mesh 50×100	0.009256	0.006699	0.003424		
	Mesh 60×120	0.005150	0.0047960	0.003412		
	Base	40%	50%	60%	Phase-field ϕ	
3D single notched tension test	Mesh 40× 80×4	0.050916	0.050090	0.050228	0.004952	
	Mesh 50×100×4	0.026872	0.026759	0.026084		
	Mesh 60×120×4	0.012637	0.011345	0.010743		

Reference List

References

Griffith, A. A. (1921). The phenomena of rupture and flow in solids. *Philos. Trans. R. Soc. Lond. A Math. Phys. Eng. Sci.*, **221**: 163–198.

Irwin, G. R. (1958). Elasticity and plasticity: fracture. *Springer Berlin Heidelberg, Berlin, Heidelber*, 551–590.

Barenblatt, G.I. (1962). The mathematical theory of equilibrium cracks in brittle fracture *Advances in Applied Mechanics*, **7**: 55–129.

Francfort, G. A. and Marigo, J. J. (1998). Revisiting brittle fracture as an energy minimization problem. *Journal of the Mechanics and Physics of Solids*, **46**: 1319–1342.

Moës, N., Dolbow, J. and Belytschko, T. (1999). A finite element method for crack growth without remeshing. *International Journal for Numerical Methods in Engineering*, **46**: 131–150.

Branco, R., Antunes, F. V., and Costa, J. D. (2015). A review on 3D-FE adaptive remeshing techniques for crack growth modelling. *Engineering Fracture Mechanics*, **141**: 170–195.

Bourdin, B., Francfort, G. A., and Marigo, J. J. (2008). The variational approach to fracture. *Journal of Elasticity*, **91**: 5–148.

Miehe, C., Welschinger, F., and Hofacker, M. (2010). Thermodynamically consistent phase-field models of fracture: Variational principles and multi-field FE implementations. *International Journal for Numerical Methods in Engineering*, **83**: 1273–1311.

Gardner Jr, E. S. (1985). Exponential smoothing: The state of the art. *Journal of Forecasting*, **4**: 1–28.

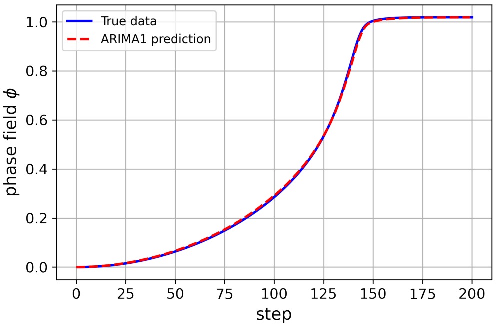

(a) Single edge notched test: $\alpha = 90^\circ$

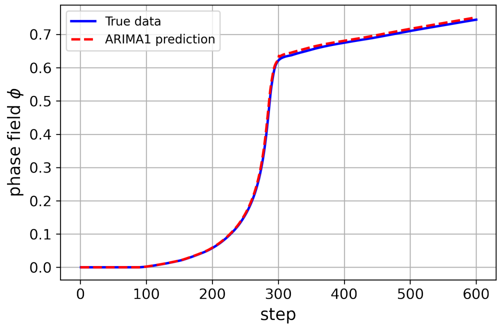

(b) Single edge notched test: $\alpha = 0$

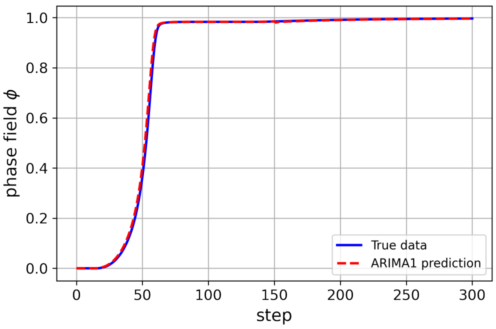

(c) Single edge notched test: $\alpha = 45^\circ$

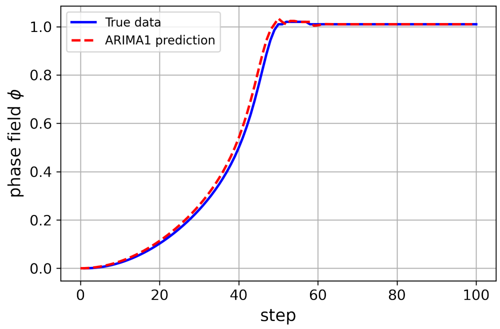

(d) Symmetric doubled notched test

Fig. 9: Training results using ARIMA1.

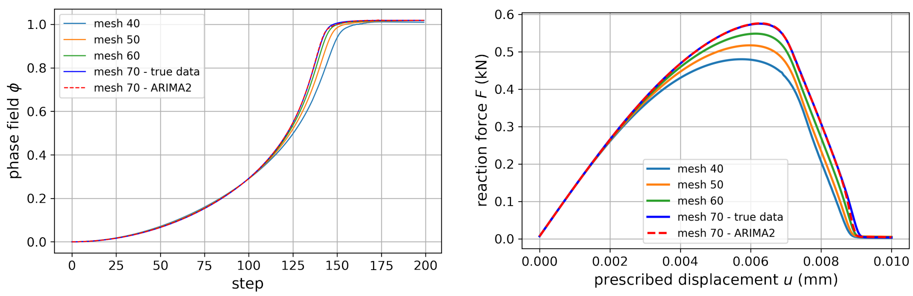

Fig. 10: Training results when $\alpha = 0$ (tension) using ARIMA2.

Brockwell, P. J., and Davis, R. A. (2002). Introduction to time series and forecasting *New York, NY: Springer New York*.

Molnár, G., and Gravouil, A. (2017). 2D and 3D Abaqus implementation of a robust staggered phase-field solution for modeling brittle fracture. *Finite Elements in Analysis and Design*, **130**: 27–38.

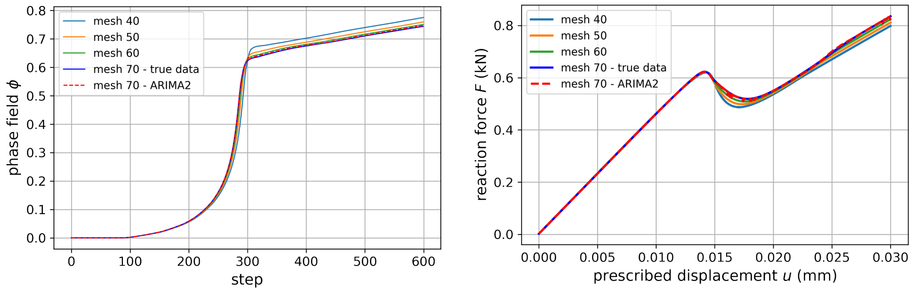

Fig. 11: Training results when $\alpha = 90^\circ$ (shear) using ARIMA2.

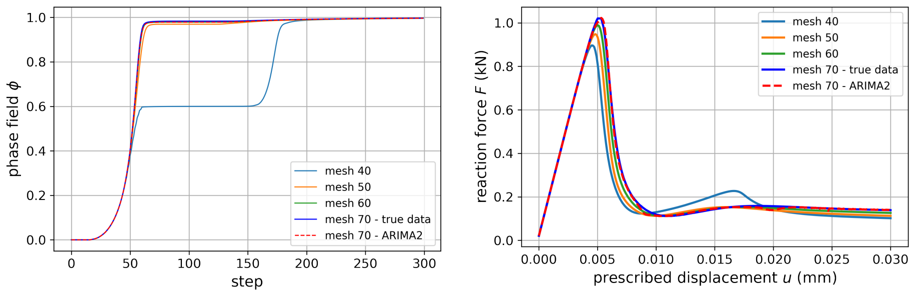

Fig. 12: Training results when $\alpha = 45^\circ$ (mixed-mode) using ARIMA2.

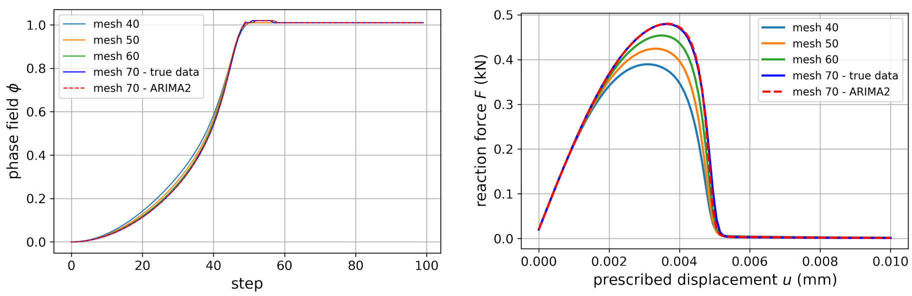

Fig. 13: Training results for the double-notch problem using ARIMA2.

Singh, N., Verhoosel, C. V., De Borst, R., and Van Brummelen, E. H. (2016). A fracture-controlled path-following technique for phase-field modeling of brittle fracture. *Finite Elements in Analysis and Design*, **113**: 14–29.

Dinh, M. N., Vo, C. T., Nguyen, C. T., and La, N. M. (2022). Phase-Field modelling of brittle fracture using time-series forecasting. *In Computational Science–ICCS 2022: 22nd International Conference, London, UK, June 21–23, 2022, Proceedings*, **Part II**:

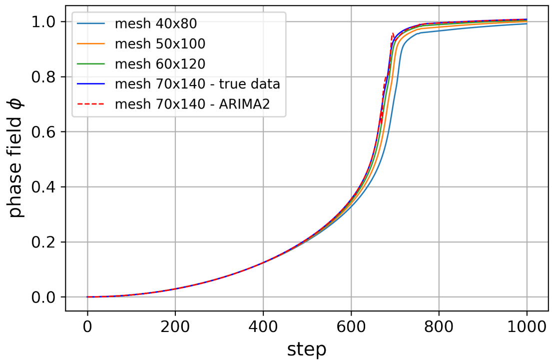

Fig. 14: Training results for the three-dimensional problem using ARIMA2.

266-274.

Ghaffari Motlagh, Y., Jimack, P. K., and de Borst, R. (2022). Deep learning phase-field model for brittle fractures. *International Journal for Numerical Methods in Engineering*, 1–19.

Hughes, T. J. (2012). The finite element method: linear static and dynamic finite element analysis. *Courier Corporation.*

Miehe, C., Welschinger, F., and Hofacker, M. (2010). Thermodynamically consistent phase-field models of fracture: Variational principles and multi-field FE implementations. *International Journal for Numerical Methods in Engineering*, **83**: 1273–1311.

Hamilton, J. D. (2020). Time series analysis. *Princeton university press.*